Editors' Suggestion

Backscatter-Immune Injection-Locked Brillouin Laser in Silicon

Nils T. Otterstrom,[1,2,*] Shai Gertler,[1] Yishu Zhou,[1] Eric A. Kittlaus,[1,3] Ryan O. Behunin,[4,5] Michael Gehl,[2] Andrew L. Starbuck,[2] Christina M. Dallo,[2] Andrew T. Pomerene,[2] Douglas C. Trotter,[2] Anthony L. Lentine,[2] and Peter T. Rakich[1,†]

[1] *Department of Applied Physics, Yale University, New Haven, Connecticut 06520, USA*
[2] *Photonic and Phononic Microsystems, Sandia National Laboratories, Albuquerque, New Mexico 87123, USA*
[3] *Jet Propulsion Laboratory, California Institute of Technology, Pasadena, California 91101, USA*
[4] *Department of Applied Physics and Materials Science, Northern Arizona University, Flagstaff, Arizona 86011, USA*
[5] *Center for Materials Interfaces in Research and Applications, Northern Arizona University, Flagstaff, Arizona 86011, USA*

(Received 26 March 2020; revised 2 September 2020; accepted 3 September 2020; published 22 October 2020)

As self-sustained oscillators, lasers possess the unusual ability to spontaneously synchronize. These nonlinear dynamics are the basis for a simple yet powerful stabilization technique known as injection locking, in which a laser's frequency and phase can be controlled by an injected signal. Because of its inherent simplicity and favorable noise characteristics, injection locking has become a workhorse for coherent amplification and high-fidelity signal synthesis in applications ranging from precision atomic spectroscopy to distributed sensing. Within integrated photonics, however, these injection-locking dynamics remain relatively untapped—despite significant potential for technological and scientific impact. Here, we demonstrate injection locking in a silicon photonic Brillouin laser. Injection locking of this monolithic device is remarkably robust, allowing us to tune the laser emission by a significant fraction of the Brillouin gain bandwidth. Harnessing these dynamics, we demonstrate amplification of small signals by more than 23 dB. Moreover, we demonstrate that the injection-locking dynamics of this system are inherently nonreciprocal, yielding unidirectional control and backscatter immunity in an all-silicon system. This device physics opens the door to strategies for phase-noise reduction, low-noise amplification, and backscatter immunity in silicon photonics.

DOI: 10.1103/PhysRevApplied.14.044042

I. INTRODUCTION

Precise control over a laser's frequency and phase lies at the core of many important photonic applications, ranging from clock recovery in coherent optical communication [1] to high-precision atomic spectroscopy [2]. As a means of synchronizing oscillators, injection locking offers an elegant and simple approach to achieve this level of control in optical systems. In contrast to optical phase-locked loops [3,4], injection-locking schemes require no external feedback or complex locking electronics [5]; rather, it is the nonlinearity intrinsic to the self-sustained laser oscillator that permits synchronization [6–8].

First demonstrated in nonlinear electronic oscillators for efficient microwave amplification, stable high-power oscillators, and clock recovery [6,9], these dynamics have been adapted to an array of other laser [7,10,11] and optomechanical oscillators, including diode lasers [12], distributed feedback lasers [13], and toroidal optomechanical oscillators [14,15]. Within these systems, injection locking permits coherent, low-noise amplification and phase-noise reduction [15,16], enabling narrow-linewidth laser emission [17], heterodyne-based filters [18], signal synthesis for atomic physics [2,19,20], low-noise microwave generation [21–23], improved distributed sensing [24], and high-performance microwave-photonic links [25]. As many photonic technologies migrate to integrated platforms, the inherent simplicity of this method is compelling for implementation in chip-scale photonics [26], where space, bandwidth, and power consumption are constrained. In particular, implementation of injection locking within emerging silicon-based lasers would greatly augment the application space, opening the door to efficient low-noise amplification for applications ranging from chip-scale atomic clocks to coherent communications.

With the potential for tunable, low-noise emission, Brillouin lasers are an intriguing candidate system for injection locking. To date, however, injection-locked operation and control has yet to be demonstrated in these systems; moreover, it is not clear whether the dynamics of conventional Brillouin lasers would be compatible

*ntotter@sandia.gov
†peter.rakich@yale.edu

with such techniques. In this context, the recent emergence of silicon-based Brillouin lasers—which exhibit a set of intriguing and unusual properties [27]—unlock alternative opportunities for injection-locked Brillouin technologies. Thanks to radically enhanced (greater than 1000 times that of fiber) and highly tailorable nonlinearities based on forward intermodal Brillouin scattering [28], these all-silicon laser systems are ideally suited for injection-locked operation, with dynamics that intrinsically preserve coherence, avoid the need for on-chip circulators or isolators, prevent unwanted cascading, and support modal degrees of freedom for independent control of the pump field and laser emission. Combining these unique characteristics with powerful injection-locking techniques could be the first step towards tunable, highly coherent laser emission, efficient on-chip amplification, backscatter immunity, and high-fidelity single-sideband modulation for on-chip signal processing and atomic physics demonstrations.

Here, we demonstrate injection locking of a silicon Brillouin laser. This system provides robust and flexible injection-locking dynamics with lock ranges up to 1.8 MHz and the ability to amplify signals by more than 23 dB. The unique combination of spatial and temporal dynamics of this Brillouin laser permit synchronization of light fields with near perfect fidelity, reducing low-frequency phase noise by more than 50 dB over a large bandwidth. Moreover, we show that, due to the traveling-wave nature of the Brillouin gain process, injection locking of this system is intrinsically unidirectional, demonstrating that the laser oscillation is inherently impervious to unwanted backscatter. We demonstrate this physics with devices fabricated from both standard electron-beam lithography and CMOS-foundry photolithography. We show that these micron-scale Brillouin-active devices are ideally suited to large-scale photolithographic processes, permitting enhanced performance, uniformity, and yield. This work highlights the CMOS compatibility of silicon Brillouin photonic systems and paves the way for coherent clock recovery, low-noise amplification, and backscatter-immune laser systems within integrated photonics.

II. RESULTS

We leverage a flexible intermodal Brillouin laser concept to demonstrate injection-locked lasing in a CMOS-compatible device platform. Building on recent demonstrations of Brillouin lasing [27] and resonantly enhanced amplification in silicon [29], the device is composed of a multimode silicon racetrack cavity with two Brillouin-active suspended regions, as shown in Fig. 1(a).Throughout the device, the racetrack waveguide supports guidance of TE-like symmetric and antisymmetric optical modes, which yield two distinct sets of high-Q resonances centered at $\{\omega_1^n\}$ and $\{\omega_2^m\}$, respectively [see Fig. 1(d)]. Within the Brillouin-active segments [30–32], a 6-GHz antisymmetric elastic wave mediates large Brillouin coupling between the symmetric and antisymmetric spatial modes through stimulated intermodal Brillouin scattering [28,33,34]. This phase-matched process provides mode-selective single-sideband gain [28], which permits flexible and robust laser oscillation [27].

In order to precisely control the intermodal nonlinear gain and laser emission, we interface this laser geometry with up to three directional couplers that are designed to provide mode-specific coupling, as illustrated in Fig. 1(a). Couplers A and B (labeled MC1) produce high-contrast input and output coupling to the symmetric cavity modes (with as low as -40 dB of crosstalk), while mode-selective coupler C (MC2) preferentially couples to the antisymmetric cavity modes, with contrast that can be designed to range from 10 to 25 dB of symmetric mode rejection (for details, see Appendices B and C). As shown in Fig. 1(d), efficient laser oscillation at ω_e occurs when the pump wave is tuned to an antisymmetric cavity resonance ω_2^m that is detuned from a symmetric cavity mode ω_1^n by the Brillouin frequency Ω_B. When the pump power is sufficient to achieve laser oscillation, we inject a seed wave into a symmetric cavity mode and tune its frequency ω_s through the natural laser emission frequency $\omega_e = \omega_p - \Omega_B$ to produce injection-locked Brillouin lasing at ω_s.

We characterize the injection-locking dynamics of this system using the experimental setup diagrammed in Fig. 2(a) to perform heterodyne laser spectroscopy. The apparatus directs telecom-band laser light (λ_p) along three different paths to (1) supply the pump wave of a desired power using an erbium-doped fiber amplifier and variable optical attenuator, (2) synthesize a seed at frequency $\omega_s = \omega_p - \Omega$, and (3) create an optical local oscillator (LO) at frequency $\omega_p + \Delta$ using an acousto-optic modulator (AOM) for heterodyne spectral analysis. Fiber-optic couplers and switches route the pump and seed waves on chip through grating couplers. Subsequently, the pump and seed waves are resonantly coupled into the antisymmetric and symmetric cavity modes using the mode-specific couplers and frequency selectivity of the resonator. Above threshold, the laser emission exits the resonator through coupler B toward the output grating coupler. Once off chip, this laser light is combined with the AOM-shifted optical LO and detected by a high-speed photoreceiver. In conjunction with a rf spectrum analyzer, this scheme allows us to study the heterodyne spectrum—which reveals the degree of coherence between the laser emission and the pump—with hertz-level resolution.

Using this approach, we experimentally characterize key properties of the injection-locking Brillouin dynamics as a function of frequency detuning and seed power. The upper density plots in Figs. 2(b)(i)–2(b)(iii) reveal the evolution of the power spectral density as the seed frequency ω_s is tuned through the natural laser emission frequency $\omega_p -$

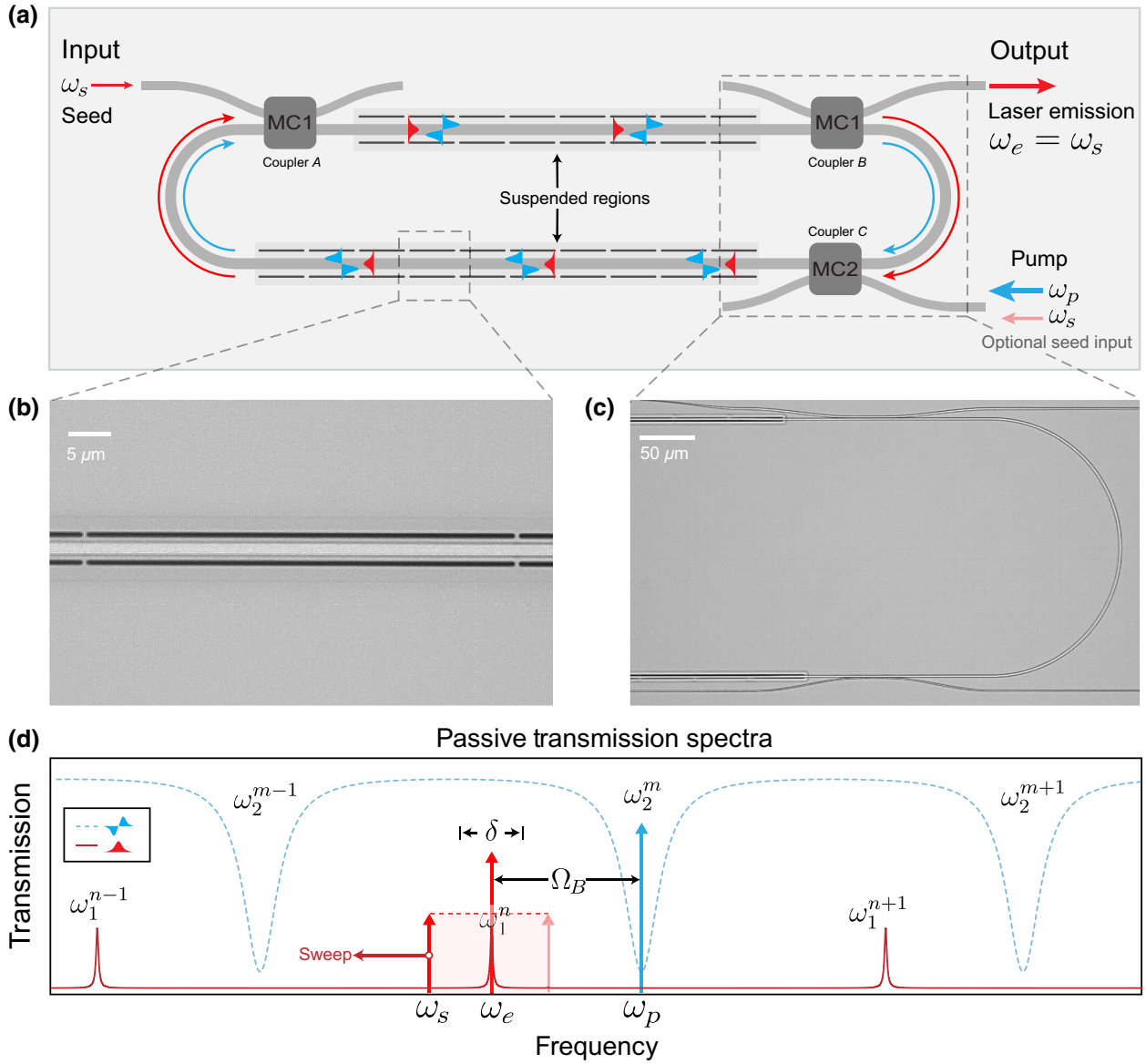

FIG. 1. (a) Schematic of device concept and operation. The Brillouin laser racetrack cavity is formed from a multimode silicon waveguide that supports symmetric (red) and antisymmetric (blue) TE-like optical spatial modes. The straight segments of the racetrack are defined by a suspended hybrid photonic-phononic waveguide that yields large intermodal Brillouin coupling. Couplers *A* and *B* (MC1) couple to the cavity modes produced by the symmetric optical spatial mode ω_1^n while mode-selective coupler 2 (MC2) is designed to couple primarily to the antisymmetric cavity modes. (b) Top-down optical micrograph (gray scale) of the suspended Brillouin-active waveguide. (c) Optical micrograph (gray scale) of the interface between the racetrack cavity and couplers *B* (MC1) and *C* (MC2). (d) Idealized transmission spectrum produced by the antisymmetric waveguide mode (dashed blue; thru port of coupler *C*) and symmetric waveguide mode (red; input at coupler *A*, output at coupler *B*). Efficient laser oscillation of the symmetric cavity mode ω_1^n occurs when the pump wave is tuned to an antisymmetric cavity mode that satisfies the Brillouin condition ($\omega_p = \omega_2^m = \omega_1^n + \Omega_B$). Laser oscillation of the symmetric mode ω_e can be phase and frequency locked by injecting a seed of sufficient power at frequency ω_s that falls within the lock range $\omega_e \pm \delta/2$. The lock range is determined experimentally by sweeping the signal frequency through the natural laser emission frequency.

Ω_B. These measurements are repeated for a set of three distinct signal powers [(i)–(iii)], and each plot is composed of a series of 38 spectral traces. As the seed frequency approaches the natural oscillation frequency, we observe a crescendo of four-wave-mixing-like scattering—manifest by many equally spaced tones—that abruptly transitions into injection-locked lasing over a lock range $\omega_e \pm \delta/2$.

Within this range, the laser emission is captured by the seed source, assuming its frequency, phase, and coherence properties. Since, in our experiments,

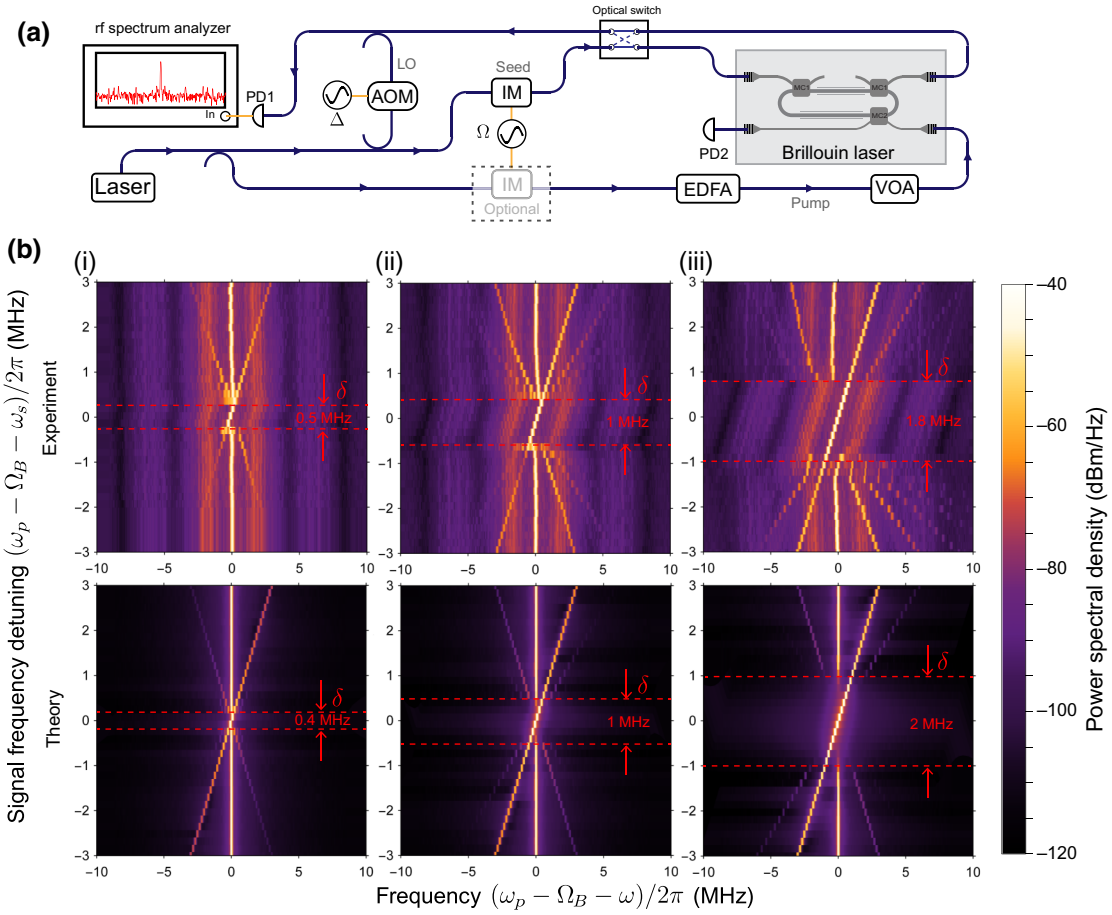

FIG. 2. (a) Experimental apparatus for injection locking and heterodyne spectroscopy. Telecom laser light is split along three paths. Along the top path, an acousto-optic frequency shifter is used to generate an optical LO of frequency $\omega_p + \Delta$, where $\Delta = 44$ MHz. Light routed to the bottom path passes through an erbium-doped fiber amplifier (EDFA) and variable optical attenuator (VOA) such that pump light of a desired power can be delivered on chip, while the middle path uses an intensity modulator to synthesize a seed at $\omega_s = \omega_p - \Omega$. Optionally, the seed can be directly synthesized as a sideband of the pump wave. Fiber-optic switches and couplers route the light on and off chip through grating couplers that interface the desired ports of the system. Light exiting the chip is combined with the optical LO and detected using a high-speed photoreceiver for heterodyne spectroscopy. (b) Measured (top) and simulated (bottom) injection-locking dynamics at three different seed powers [(i) 0.4 μW, (ii) 2.6 μW, (iii) 17 μW]. Note that the capture range expands with increasing seed power, and that Brillouin-mediated four-wave mixing can occur as the seed approaches the lock range $\omega_e \pm \delta/2$.

the seed laser is synthesized from the pump laser, its phase fluctuations are highly correlated with that of the pump field. Figures 3(a) and 3(b) contain highresolution [resolution bandwidth (RBW) = 100 Hz, RBW = 1 Hz] heterodyne spectra of the beat note between the pump and the Brillouin laser emission, revealing a highly monochromatic resolution-bandwidth-limited signal. Relative to the free-running silicon Brillouin laser (with a phonon linewidth of 1 kHz, measured by analyzing the beat note between the pump and Stokes waves) [27], this measurement demonstrates a reduction of the phonon phase noise by more than 50 dB at both 30 kHz and 10 Hz offsets. Moreover, at the lowest seed powers, injection-locked lasing yields a dramatic power enhancement of the seed source, corresponding to an effective net amplification of more than 23 dB over a lock range of 0.5 MHz. As we increase the seed power, we observe a clear enlargement of this lock range up to a maximum $\delta = 1.8$ MHz.

To understand this behavior theoretically, we perform a series of stochastic coupled-mode simulations that capture the essential locking dynamics of the system [see the bottom three plots of Fig. 2(d)]. As shown in Fig. 2(d), the lock ranges (δ) obtained from these theoretical simulations (bottom) demonstrate excellent agreement with our experimental observations. These simulations also capture the same four-wave-mixing-like dynamics when the seed frequency is in sufficient proximity of the lock range. These spectral features are a result of Brillouin-induced intermodal four-wave mixing, which is corroborated by

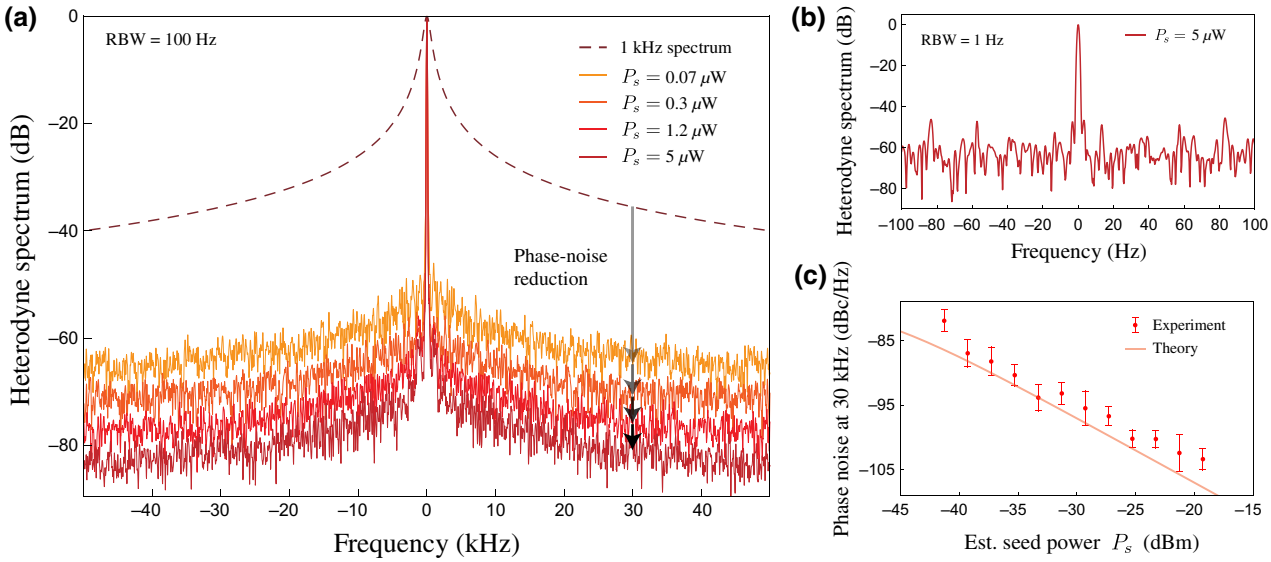

FIG. 3. (a) Optical heterodyne spectra (RBW = 100 Hz) of the injection locked Brillouin laser emission at various seed powers (detected at PD1; the local oscillator is the transmitted pump). The phase noise over a broad spectrum is monotonically reduced as the signal power is increased. Relative to phonon phase noise produced by a typical 1 kHz heterodyne spectrum (dashed dark red) of a free-running Brillouin laser [27], we achieve more than 50 dB of phase-noise suppression from 10 Hz to 50 kHz (in dBc/Hz). (b) Enlarged heterodyne spectrum (RBW = 1 Hz) of the injection-locked laser. Phase-noise reduction is most dramatic at low offset frequencies. (c) Phase noise at 30 kHz as a function of estimated seed power, demonstrating good agreement with the theoretical trend [Eq. (1)] derived in Appendix A. See Appendix A 2 for more details on the data analysis.

the fact that our simulations only include the Brillouin nonlinearity. The appearance of these new tones demonstrates that, like Kerr and Raman interactions, stimulated Brillouin scattering is also a $\chi^{(3)}$ nonlinearity [35,36] that can produce four-wave mixing.

We also develop an analytical framework to understand the degree to which injection locking improves the internal phonon linewidth, or equivalently, the coherence between the pump and Brillouin laser emission. Through injection locking, the Brillouin laser noise becomes increasingly correlated with that of the seed and consequently that of the pump laser, yielding a highly coherent heterodyne pump-Stokes beat note in which the optical phase noise cancels through common mode rejection [27]. This improved degree of coherence arises because injection locking produces an additional damping mechanism in the phase dynamics of the phonon field, further suppressing the effects of thermo-mechanical noise beyond the typical Schawlow-Townes-induced suppression [see Eq. (A20)]. Starting from the Hamiltonian-based equations of motion and including Langevin terms that are consistent with the fluctuation-dissipation theorem (for more details, see Appendix A), the phase-noise spectrum of the phonon field, or equivalently of the pump-Stokes beat note, is given by

$$\mathscr{L}(f) = \frac{\Gamma(2n_{\rm th}+1)}{4\beta^2}\frac{1}{(\pi\delta)^2+(2\pi f)^2}, \qquad (1)$$

where Γ is the phonon dissipation rate, $n_{\rm th}$ is the thermal occupation of the phonon field, β^2 is the coherent phonon number, and δ is the lock range. From Eq. (1), we observe that injection locking produces significant reduction of the phonon phase noise at low frequencies. This phase-noise reduction increases as a function of lock range—which is proportional to the seed power—as demonstrated in Fig. 3(c).

Another intriguing feature of this traveling-wave laser is that, due to well-resolved phase-matching conditions, the gain mechanism is intrinsically unidirectional [29,37], providing nonreciprocal control of the laser oscillation (see Fig. 4).We test the reciprocity of the injection locking using a fiber-optic switch, which allows us to rapidly alternate between forward and backward injection configurations [see Fig. 2(a) and Figs. 4(a) and 4(b)]. As shown in Fig. 4(a), when the seed is coupled into the resonator such that it copropagates with the self-oscillating Stokes wave, we are able to achieve injection locking. Conversely, when the seed enters in the counterpropagating direction, the laser emission is unaffected by its presence [see Fig. 4(b)(ii)], demonstrating nonreciprocal control and backscatter immunity of this monolithic silicon system.

III. DISCUSSION

In this work, we have demonstrated injection locking in an integrated Brillouin laser. The unique injection-locking dynamics of this system permit a large lock range, a high

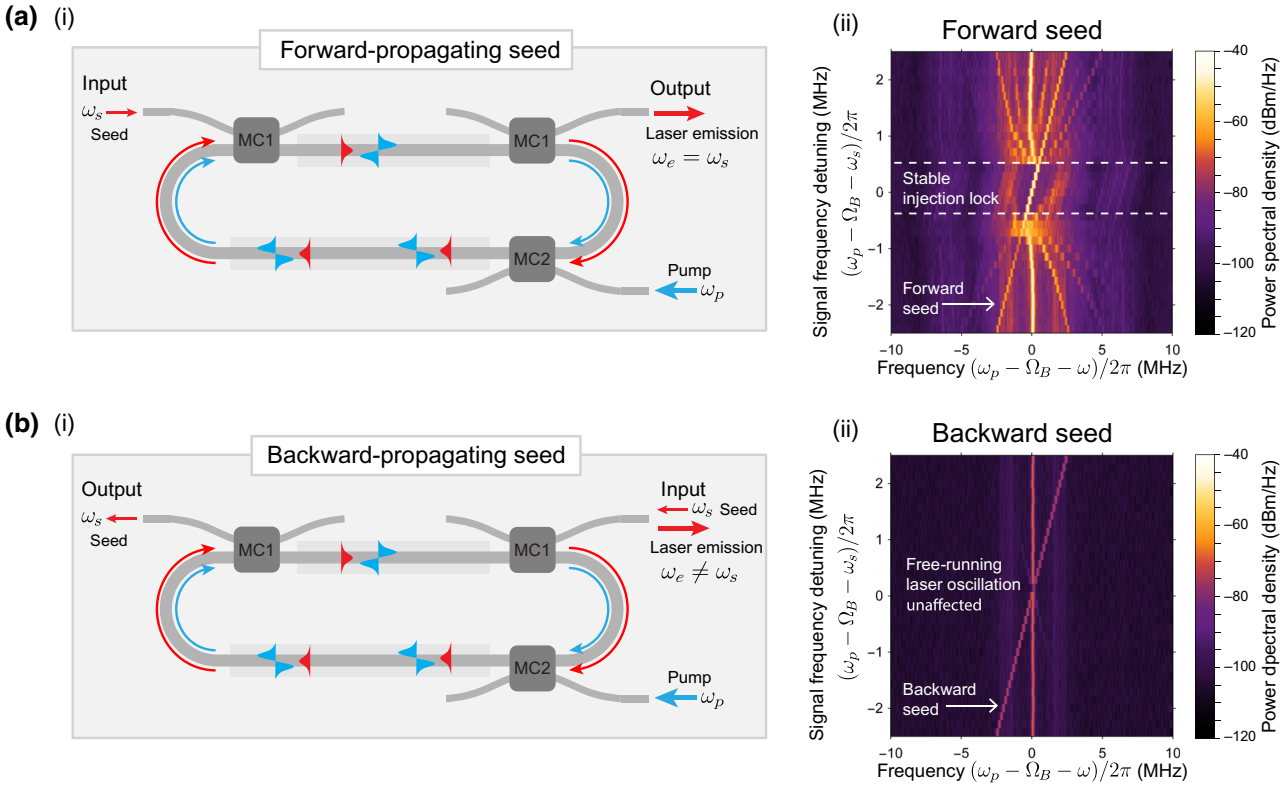

FIG. 4. Experimental demonstration of nonreciprocal injection-locking dynamics. (a)(i) Operation scheme for injection locking in the forward direction. The seed is coupled into the resonator such that it copropagates with the pump and self-oscillating Stokes mode. (a)(ii) Experimental density plot demonstrating injection locking in the forward direction. (b)(i) Seed light is injected in the backward direction such that it counterpropagates with the light in the cavity. (b)(ii) Experimental density plot demonstrating backscatter immunity. In this case, the laser emission is unaffected by the presence of the seed.

degree of phase-noise reduction, and nonreciprocal control of the laser oscillation. We fabricate devices with CMOS-compatible techniques and achieve this performance without the use of locking electronics, demonstrating the potential for practical implementation in scalable photonic systems. Looking forward, these results are a stepping stone toward clock distribution, low-noise signal amplification, and backscatter immunity in integrated photonics.

A salient property of this injection-locked Brillouin laser is the ability to reduce the phonon phase noise by orders of magnitude (more than 50 dB). Thanks to the unconventional separation of time scales between the optical and acoustic fields [27], the internal dynamics of this silicon-based laser system are uniquely suited to this phase coherent process. In particular, the free-running laser emission can be viewed as a frequency-shifted version of the input pump laser, with modest levels of residual phase noise (1 kHz linewidth) due to the presence of thermal phonons [27]. Here we show that injection locking can be used to significantly reduce this source of phase noise. When the seed source is synthesized from the pump laser, injection locking forces the Brillouin laser emission to assume an even greater degree of coherence with the pump laser, further suppressing the effects of thermo-mechanical fluctuations. Thus, as the strength of the injection-locking process increases (i.e., the seed power increases), the phonon phase noise continues to decrease to a value that is ultimately limited by the excess noise of the seed source (less than −105 dBc/Hz at 10 kHz, synthesized using an Agilent rf source E8257D), which is below the measured phase noise of this system. Given these properties, the injection locked Brillouin laser may serve as both a narrowband (less than 1 MHz) optical filter and low-noise amplifier in the context of coherent optical communications, enabling high-fidelity carrier recovery [38] of data-laden signals and high-performance optical signal processing schemes [39]. Moreover, by tuning the optical resonances using silicon photonic integrated heaters [40], this narrowband functionality is readily reconfigurable across the c band.

This form of coherent amplification may prove advantageous for a range of integrated photonic functionalities. Phase coherence between the input seed and output laser enables the coherent addition of multiple injection locked sources, provided they are locked to the same input source. In this way, the overall output power may be greatly

enhanced by creating an array of injection-locked Brillouin lasers and coherently combining them.

Single-sideband (SSB) modulation may be another compelling use for this device physics. SSB modulators are crucial components for communications and spectroscopy applications, but typically require a complex system comprised of many photonic modulators and phase shifters [41]. Here, through the phase-matching conditions of the intermodal Brillouin process, we can achieve single-sideband emission with high contrast (more than 50 dB of anti-Stokes suppression; see Appendix C). Additionally, through the design of our mode-specific couplers, we can reject the pump wave by more than 45 dB. Thus, in combination with mature silicon photonic intensity modulators, an injection-locked Brillouin laser opens the door to coherent single-sideband modulation (over a modest approximate 1 MHz bandwidth) with significant carrier and sidemode suppression. At the same time, this injection-locked Brillouin laser system complements existing single-sideband modulator technologies [41] by providing a means to suppress unwanted spurious signals.

Furthermore, the unique properties of this Brillouin system open the door to an intriguing set of nonreciprocal all-silicon photonic devices. Here, we show that the injection locking is intrinsically unidirectional; a seed entering the device in the forward direction (copropagating with the laser emission) locks the laser output, while a seed injected in the backward direction does not. This result demonstrates both nonreciprocal control and backscatter immunity. As a nonreciprocal element, this system permits unidirectional power enhancement of more than 23 dB. At the same time, these measurements show that the Brillouin laser itself, through unidirectional mode conversion, prevents unwanted backscatter from reaching the original pump source. In this way, the silicon Brillouin laser can be viewed as a frequency-shifting isolator, with an insertion loss given by the laser efficiency. These capabilities offer a complementary approach to time-modulation-based [37,42–48] and magneto-optic integration strategies [49,50] for robust on-chip nonreciprocal technologies.

In summary, we have demonstrated injection-locked Brillouin lasing in an all-silicon device. This monolithically integrated Brillouin laser exhibits a range of powerful injection-locking dynamics, yielding dramatic phase-noise reduction (relative to that of the free-running laser oscillator), high-gain power enhancement of small signals, and backscatter immunity. As optical technologies trend toward integrated platforms, these results open the door to a range of accessible amplifier, modulator, and nonreciprocal technologies in emerging photonic systems.

ACKNOWLEDGMENTS

We thank Prashanta Kharel and Freek Ruesink for valuable discussions and feedback.

This material is based upon work supported by the Packard Fellowship for Science and Engineering, the National Science Foundation Graduate Research Fellowship under Grant No. DGE1122492 (N.T.O.), and the Laboratory Directed Research and Development program at Sandia National Laboratories. Sandia National Laboratories is a multiprogram laboratory managed and operated by the National Technology and Engineering Solutions of Sandia, LLC, a wholly owned subsidiary of Honeywell International, Inc., for the U.S. Department of Energy's National Nuclear Security Administration under Contract No. DE-NA-0003525. Part of the research was carried out at the Jet Propulsion Laboratory, California Institute of Technology, under a contract with the National Aeronautics and Space Administration. This paper describes objective technical results and analysis. Any subjective views or opinions that might be expressed in the paper do not necessarily represent the views of the U.S. Department of Energy, the National Science Foundation, the National Aeronautics and Space Administration, or the United States Government.

APPENDIX A: RELATIVE INTENSITY NOISE AND PHASE-NOISE REDUCTION

In this section, we derive the fundamental relative intensity noise (RIN) and phase-noise reduction properties produced by injection-locked Brillouin lasing. The mean-field equations of motion for the silicon Brillouin laser are given by [27,29]

$$\dot{a}_s(t) = -i\omega_1^n a_s(t) - \frac{\gamma_{\mathrm{tot},1}}{2} a_s(t) - ig^* a_p(t) b^\dagger(t) + \sqrt{\gamma_{A,1}} S^{\mathrm{in}}(t), \tag{A1a}$$

$$\dot{b}(t) = -i\Omega_B b(t) - \frac{\Gamma}{2} b(t) - ig^* a_p(t) a_s^\dagger(t) + \eta(t), \tag{A1b}$$

$$\dot{a}_p(t) = -i\omega_2^m a_p(t) - \frac{\gamma_{\mathrm{tot},2}}{2} a_p(t) - iga_s(t) b(t) + \sqrt{\gamma_{C,2}} S_p^{\mathrm{in}}(t), \tag{A1c}$$

where $a_s(t)$, $b(t)$, and $a_p(t)$ are the coupled-mode amplitudes for the Stokes, phonon, and pump fields, respectively, with units of $[\sqrt{\text{number}}]$, $\dot{a}_s(t)$, $\dot{b}(t)$, and $\dot{a}_p(t)$ are the time derivatives of these same fields, $S^{\mathrm{in}}(t)$ and $S_p^{\mathrm{in}}(t)$ represent the input seed and pump-wave fields (with units $[\sqrt{\text{number} \times \text{Hz}}]$), and $\eta(t)$ is the mechanical stochastic driving term that is consistent with the fluctuation-dissipation theorem, with a two-time correlation function of $\langle \eta(t')\eta^\dagger(t)\rangle = \Gamma(n_{\mathrm{th}} + 1)\delta(t - t')$, where n_{th} is the thermal occupation of the phonon field and Γ is the phonon dissipation rate. We denote the Hermitian conjugate with "†" and use "*" for the complex conjugate. Here, g is the Brillouin coupling rate (related to the Brillouin gain coefficient by $G_B = 4|g|^2|a_p|^2/P_p\Gamma v_{g,1}$, where P_p is the pump power and $v_{g,1}$ is the group velocity of the first spatial mode), $\gamma_{(A,B,C),(1,2)}$ are the dissipation rates produced

by couplers A, B, or C (see Fig. 1 of the main text) for light propagating in the symmetric (1) or antisymmetric (2) spatial modes, and $\gamma_{\mathrm{tot},(1,2)}$ are the total dissipation rates associated with resonant symmetric (ω_1^n) and antisymmetric modes (ω_2^m). Since the system is dominated by the thermal noise of the phonon field, for simplicity, we neglect optical vacuum fluctuations.

We next move to the rotating frame by substituting the slowly varying envelopes $\bar{a}_s(t)$, $\bar{b}(t)$, and $\bar{a}_p(t)$, which are defined by $a_s(t) = \bar{a}_s(t)\exp(-i\omega_s t)$, $a_p(t) = \bar{a}_p(t)\exp(-i\omega_p t)$, and $b(t) = \bar{b}(t)\exp(-i\Omega t)$. The terms $\bar{\eta}(t)$, $\bar{S}^{\mathrm{in}}(t)$, and $\bar{S}_p^{\mathrm{in}}(t)$ are shifted in like manner. This transformation yields

$$\dot{\bar{a}}_s(t) = i(\omega_s - \omega_1^n)\bar{a}_s(t) - \frac{\gamma_{\mathrm{tot},1}}{2}\bar{a}_s(t) - ig^*\bar{a}_p(t)\bar{b}^\dagger(t) + \sqrt{\gamma_{A,1}}\bar{S}^{\mathrm{in}}(t), \tag{A2a}$$

$$\dot{\bar{b}}(t) = i(\Omega - \Omega_B)\bar{b}(t) - \frac{\Gamma}{2}\bar{b}(t) - ig^*\bar{a}_p(t)\bar{a}_s^\dagger(t) + \bar{\eta}(t), \tag{A2b}$$

$$\dot{\bar{a}}_p(t) = i(\omega_p - \omega_2^m)\bar{a}_p(t) - \frac{\gamma_{\mathrm{tot},2}}{2}\bar{a}_p(t) - ig\bar{a}_s(t)\bar{b}(t) + \sqrt{\gamma_{C,2}}\bar{S}_p^{\mathrm{in}}(t), \tag{A2c}$$

where conservation of energy requires $\omega_p = \omega_s + \Omega_B$.

We can study the time dynamics and noise properties of the system by applying the appropriate separation of time scales. In this silicon Brillouin system, there is a well-defined dissipation hierarchy between the pump, Stokes, and phonon fields (given by $\gamma_{\mathrm{tot},2} \gg \gamma_{\mathrm{tot},1} \gg \Gamma$, respectively), which allows us to adiabatically eliminate the pump and Stokes fields as

$$\begin{aligned}\bar{a}_p &= \frac{2}{\gamma_{\mathrm{tot},2}}(-ig\bar{a}_s\bar{b} + \sqrt{\gamma_{C,2}}\bar{S}_p^{\mathrm{in}}),\\ \bar{a}_s &= \frac{\chi_s[\sqrt{\gamma_{A,1}}\bar{S}^{\mathrm{in}} - 2ig^*\sqrt{\gamma_{C,2}}\bar{S}_p^{\mathrm{in}}/\gamma_{\mathrm{tot},2}\bar{b}^\dagger]}{1 + 2|g|^2|\bar{b}|^2\chi_s/\gamma_{\mathrm{tot},2}},\end{aligned} \tag{A3}$$

where the Stokes susceptibility χ_s is given by $\chi_s = [-i(\omega_s - \omega_1^n) + \gamma_{\mathrm{tot},1}/2]^{-1}$ and we have taken the pump to be on resonance (i.e., $\omega_p = \omega_2^m$). Inserting these expressions into Eqs. (A2) yields the following nonlinear equation of motion for the phonon degrees of freedom:

$$\dot{\bar{b}}(t) = Q(t)\bar{b}(t)^2 + M(t)\bar{b}(t) + W(t) + \bar{\eta}(t). \tag{A4}$$

Here $Q(t)$, $M(t)$, $W(t)$, and $\sigma(t)$ are defined as

$$Q(t) = -\sigma(t)\left[\frac{2ig|g|^2|\chi_s|^2\sqrt{\gamma_{A,1}\gamma_{C,2}}\bar{S}_p^{\mathrm{in}*}\bar{S}^{\mathrm{in}}}{\gamma_{\mathrm{tot},2}}\right], \tag{A5a}$$

$$M(t) = i(\Omega - \Omega_B) - \frac{\Gamma}{2} - \sigma(t) \times \left[|\chi_s|^2|g|^2\gamma_{A,1}|S^{\mathrm{in}}|^2 - \frac{2|g|^2\gamma_{C,2}|S_p^{\mathrm{in}}|^2\chi_s^*}{\gamma_{\mathrm{tot},2}}\right], \tag{A5b}$$

$$W(t) = \sigma(t)\left[-ig^*\chi_s^*\sqrt{\gamma_{A,1}\gamma_{C,2}}\bar{S}^{\mathrm{in}*}S_p^{\mathrm{in}}\right], \tag{A5c}$$

$$\sigma(t) = \frac{2}{\gamma_{\mathrm{tot},2}|1 + 2|g|^2|\bar{b}(t)|^2\chi_s/\gamma_{\mathrm{tot},2}|^2}. \tag{A5d}$$

To separately analyze the RIN and phase noise produced by laser oscillation, we express $\bar{b}(t)$ as

$$\bar{b}(t) = [\beta + \delta\beta(t)]e^{i\phi(t)}, \tag{A6}$$

where real-valued $\delta\beta(t)$ and $\phi(t)$ represent the intrinsic zero-mean amplitude and phase fluctuations of the laser system, respectively. Inserting this expression into Eqs. (A5), we find that

$$\begin{aligned}&\delta\dot{\beta}(t)e^{i\phi(t)} + i\dot{\phi}(t)[\beta + \delta\beta(t)]e^{i\phi(t)}\\ &\quad= Q(t)[\beta + \delta\beta(t)]^2e^{2i\phi(t)} + M(t)[\beta + \delta\beta(t)]e^{i\phi(t)}\\ &\qquad+ W(t) + \bar{\eta}(t).\end{aligned} \tag{A7}$$

Assuming resonant conditions (i.e., $\omega_s = \omega_2^n$) and considering the relative phases between $W(t)$ and $Q(t)$, we can rewrite these expressions as

$$W(t) = |W(t)|e^{i\phi_0}, \qquad Q(t) = -|Q(t)|e^{-i\phi_0}, \tag{A8}$$

where the time-independent phase ϕ_0 is defined as $\phi_0 = \arg[-ig^*S^{\mathrm{in}*}S_p^{\mathrm{in}}]$. As such, Eq. (A7) can be reexpressed as

$$\begin{aligned}&\delta\dot{\beta}(t) + i\dot{\phi}(t)[\beta + \delta\beta(t)]\\ &\quad= -|Q(t)|[\beta + \delta\beta(t)]^2e^{i[\phi(t)-\phi_0]} + M(t)[\beta + \delta\beta(t)]\\ &\qquad+ |W(t)|e^{-i(\phi(t)-\phi_0)} + \bar{\eta}(t).\end{aligned} \tag{A9}$$

Here, we have used the fact that the Langevin term $\bar{\eta}(t)$ is uncorrelated with $e^{-i\phi(t)}$. To further simplify the equation, we expand $e^{i[\phi(t)-\phi_0]}$ to first order as $e^{i[\phi(t)-\phi_0]} \approx 1 + i[\phi(t) - \phi_0]$, yielding

$$\begin{aligned}&\delta\dot{\beta}(t) + i\dot{\phi}(t)[\beta + \delta\beta(t)]\\ &\quad= -|Q(t)|[\beta + \delta\beta(t)]^2\{1 + i[\phi(t) - \phi_0]\}\\ &\qquad+ M(t)[\beta + \delta\beta(t)]\\ &\qquad+ |W(t)|\{1 - i[\phi(t) - \phi_0]\} + \bar{\eta}(t).\end{aligned} \tag{A10}$$

1. Relative intensity noise reduction

We first seek to find the relative intensity noise, which is defined by

$$\mathrm{RIN} \equiv \frac{1}{P^2}\int_{-\infty}^{\infty} d\tau \langle \delta P(t+\tau)\delta P(t)\rangle e^{i2\pi f\tau}, \tag{A11}$$

where P is the power and $\delta P(t)$ are the zero-mean power fluctuations.

For this analysis, we Taylor expand $\sigma(t)$ to first order—using $\delta\beta(t) \ll \beta$—to isolate time-independent and time-dependent parts such that

$$\sigma(t) \approx \sigma - \sigma_{\mathrm{RIN}}\delta\beta(t), \tag{A12}$$

where σ and σ_{RIN} are defined as

$$\begin{aligned}\sigma &= \frac{2}{\gamma_{\mathrm{tot},2}|1+4|g|^2\beta^2/(\gamma_{\mathrm{tot},2}\gamma_{\mathrm{tot},1})|^2},\\ \sigma_{\mathrm{RIN}} &= \frac{4\gamma_{\mathrm{tot},1}^2|g|^2\beta}{\gamma_{\mathrm{tot},2}^2\left(\gamma_1/2+2|g|^2\beta^2/\gamma_{\mathrm{tot},2}\right)^3}.\end{aligned} \tag{A13}$$

Under this approximation, $Q(t)$, $W(t)$, and $M(t)$ [defined by Eqs. (A5a)–(A5c)] can be expressed as

$$Q(t) = Q\left(1-\frac{\sigma_{\mathrm{RIN}}\delta\beta(t)}{\sigma}\right), \tag{A14a}$$

$$W(t) = W\left(1-\frac{\sigma_{\mathrm{RIN}}\delta\beta(t)}{\sigma}\right), \tag{A14b}$$

$$M(t) = M - \frac{\sigma_{\mathrm{RIN}}[M - i(\Omega-\Omega_B)+\Gamma/2]}{\sigma}\delta\beta(t), \tag{A14c}$$

where Q, W, and M are the time-independent contributions of $Q(t)$, $W(t)$, and $M(t)$ [i.e., take definitions with $\sigma(t) \to \sigma$ in Eq. (A5d)].

To analyze the RIN reduction permitted by injection locking, we apply these expressions and isolate the real part of Eq. (A10), which yields

$$\delta\dot{\beta}(t) = \beta + |Q|\beta^2 + |W| - \frac{\Gamma_{\mathrm{RIN}}}{2}\delta\beta(t) + \frac{\bar{\eta}(t)+\bar{\eta}^\dagger(t)}{2}, \tag{A15}$$

where $[\bar{\eta}(t)+\bar{\eta}^\dagger(t)]/2$ is the real part of the Langevin term $\eta(t)$ and the amplitude fluctuation decay rate Γ_{RIN} is given by

$$\Gamma_{\mathrm{RIN}} = \frac{\sigma_{\mathrm{RIN}}}{\sigma}\left(\beta\Gamma - 2|Q|\beta^2 + 2|W| + \frac{4\beta|Q|\sigma}{\sigma_{\mathrm{RIN}}}\right). \tag{A16}$$

We have also used the fact that the real part of M ($\mathrm{Re}[M]$) is zero above threshold (i.e., gain balances total loss).

Now, solving Eq. (A15) we find that

$$\delta\beta(t) = \int_{-\infty}^{t} dt'\left[-|Q|\beta^2 + |W| + \frac{\bar{\eta}(t')+\bar{\eta}^\dagger(t')}{2}\right] \times e^{-(\Gamma_{\mathrm{RIN}}/2)(t-t')}, \tag{A17}$$

where we are integrating over the dummy variable t'.

Using the fact that $\delta\beta(t)$ is a stochastic variable with zero mean (i.e., $\langle\delta\beta(t)\rangle = 0$), we know that $-|Q|\beta^2 + |W| = 0$. Using this fact, the expression for Γ_{RIN} can be simplified as $\Gamma_{\mathrm{RIN}} = \sigma_{\mathrm{RIN}}\beta\Gamma/\sigma + 4|W|/\beta$. To find the relative intensity noise, we must evaluate $\langle\delta\beta(t+\tau)\delta\beta(t)\rangle$, which yields

$$\begin{aligned}\langle\delta\beta(t+\tau)\delta\beta(t)\rangle &= \frac{1}{4}\int_{-\infty}^{t} dt'(2n_{\mathrm{th}}+1)\Gamma e^{-(\Gamma_{\mathrm{RIN}}/2)(2t'-2t-\tau)}\\ &= \frac{\Gamma(2n_{\mathrm{th}}+1)}{4\Gamma_{\mathrm{RIN}}}[e^{-(\Gamma_{\mathrm{RIN}}/2)|\tau|}],\end{aligned} \tag{A18}$$

by using the autocorrelation function $\langle\eta(t')\eta^\dagger(t)\rangle = \Gamma(n_{\mathrm{th}}+1)\delta(t-t')$, where n_{th} is the thermal occupation of the phonon field.

Since the power $P \propto [\beta+\delta\beta(t)]^2$, the power fluctuations δP are proportional to $2\beta\delta\beta$, again assuming small amplitude fluctuations (i.e., $\delta\beta(t) \ll \beta$). As such, the RIN becomes

$$\begin{aligned}\mathrm{RIN} &\equiv \frac{1}{P^2}\int_{-\infty}^{\infty} d\tau\langle\delta P(t+\tau)\delta P(t)\rangle e^{i2\pi f\tau}\\ &= \frac{4}{\beta^2}\int_{-\infty}^{\infty} d\tau\langle\delta\beta(t+\tau)\delta\beta(t)\rangle e^{i2\pi f\tau}\\ &= \frac{\Gamma(2n_{\mathrm{th}}+1)}{\beta^2\Gamma_{\mathrm{RIN}}}\frac{1}{(\Gamma_{\mathrm{RIN}}/2)^2+(2\pi f)^2},\end{aligned} \tag{A19}$$

which is the central result of this section. We observe that the RIN spectrum is defined by a characteristic Lorentzian shape with a FWHM given by $\Gamma_{\mathrm{RIN}} = \sigma_{\mathrm{RIN}}\beta\Gamma/\sigma + 4|W|/\beta$, where $\sigma_{\mathrm{RIN}}\beta\Gamma/\sigma$ is the intrinsic damping for the amplitude fluctuations (consistent with Supplementary Section 1.4.1 of Ref. [27]) and $4|W|/\beta$ is the additional damping due to injection locking ($|W|$ is proportional to the input seed strength). Hence, the injection-locking dynamics further reduce the RIN at low frequencies. This reduction is enhanced by increasing the seed power.

2. Phase-noise reduction

We now consider the phase-noise reduction of the system when injection locked. Taking the imaginary part of

Eq. (A10), we find that

$$\dot{\phi}(t) = \left[|Q|\beta + \frac{|W|}{\beta}\right][\phi_0 - \phi(t)] + \frac{\bar{\eta}(t) - \bar{\eta}^\dagger(t)}{2i\beta}, \tag{A20}$$

which yields the solution

$$\phi(t) = \phi_0 + \int_{-\infty}^{t} dt' \left[\frac{\bar{\eta}(t') - \bar{\eta}^\dagger(t')}{2i\beta}\right] e^{-[|Q|\beta+|W|/\beta](t-t')}. \tag{A21}$$

With the solution to the phase fluctuations $\phi(t)$, we find the autocorrelation function

$$\langle\phi(t+\tau)\phi(t)\rangle = \frac{\Gamma(2n_{\rm th}+1)}{8\beta^2[|Q|\beta + |W|/\beta]} e^{-[|Q|\beta+|W|/\beta]|\tau|}, \tag{A22}$$

where we have again used the autocorrelation function $\langle\eta(t')\eta^\dagger(t)\rangle = \Gamma(n_{\rm th}+1)\delta(t-t')$ for the Langevin driving term. This yields the phase noise

$$\begin{aligned}\mathscr{L}(f) &\equiv \int_{-\infty}^{\infty} d\tau \langle\phi(t+\tau)\phi(t)\rangle e^{i2\pi f\tau} \\ &= \frac{\Gamma(2n_{\rm th}+1)}{4\beta^2} \frac{1}{(2|W|/\beta)^2 + (2\pi f)^2}.\end{aligned} \tag{A23}$$

We note that, as before, we have used the relationship $-|Q|\beta^2 + |W| = 0$. From Eq. (A23), we infer the lock range to be the FWHM of the phase-noise spectrum such that $\delta = 2|W|/(\pi\beta)$ [9]. Thus, taking the limit as $f \to 0$, the phase noise is given by

$$\begin{aligned}\mathscr{L}(0) &= \frac{\Gamma(2n_{\rm th}+1)}{16|W|^2} \\ &= \frac{2n_{\rm th}+1}{16G_B P_p v_g[\gamma_{A,1}P_s/(\hbar\omega_s\gamma_{{\rm tot},1}^2)]},\end{aligned} \tag{A24}$$

where G_B is the Brillouin gain coefficient, P_p is the intracavity pump power, v_g is the optical group velocity, and P_s is the input seed power.

From Eq. (A24), we observe that the phase-noise reduction is determined by the ratio of the thermal phonon number to the coherent seed input. In Fig. 5 we plot the phase-noise [Eq. (A23)] spectrum for four different seed powers. Increasing the seed power both enhances the overall phase-noise reduction and its bandwidth (given by the lock range), which is consistent with the behavior of injection-locked microwave oscillators [9].

Our heterodyne measurements [which are phase-noise dominated since $\beta^2 \gg \delta\beta(t)^2$] demonstrate excellent agreement with the dynamics predicted by Eq. (A23). The theoretical trend presented in Fig. 3(c) of the main text is obtained from Eq. (A23) using system parameters that are corroborated by independent measurements (including a passive characterization of the device and laser threshold conditions) and falls within the measurement uncertainty of the input seed power (which is obtained through passive ring resonator measurements and by analyzing the heterodyne spectrum when the seed frequency is well outside the lock range). Average phase noise and the error bars (i.e., standard deviation of the data in decibel scale) in Fig. 3(c) are obtained by analyzing a 1 kHz range centered around 30 kHz.

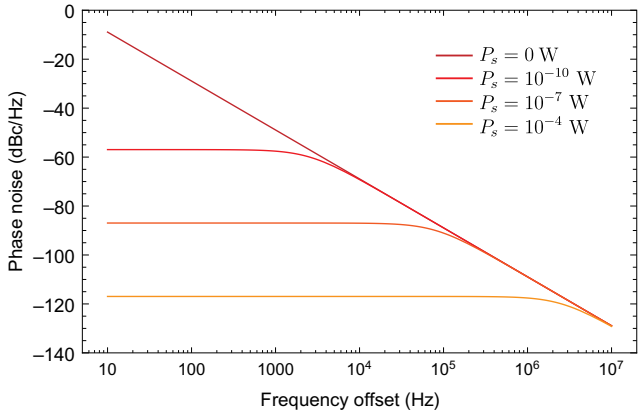

FIG. 5. Phase noise [given by Eq. (A23)] as a function of offset frequency with typical operating parameters. Note that injection locking produces phase-noise reduction over the entire lock range, which increases as a function of input seed power.

APPENDIX B: PASSIVE RESONATOR PROPERTIES

In this section, we detail the passive resonator properties of the system. In Fig. 6(a) we plot the transmission at the thru port of a three-port device fabricated through CMOS photolithography, revealing a symmetric mode quality factor of nearly 2×10^6. This spectrum also highlights the performance of mode-specific coupler MC1 [as shown in Fig. 1(a) of the main text], which preferentially couples to the antisymmetric spatial mode. Fitting the spectrum, we obtain a mode selectivity of more than 23 dB.

APPENDIX C: PUMP AND ANTI-STOKES SUPPRESSION

Because of the intrinsic phase-matching-induced symmetry breaking of the stimulated intermodal Brillouin scattering process and high selectivity of the mode-specific couplers, we are able to achieve record anti-Stokes and pump suppression in this monolithic silicon laser system. In Fig. 7 we plot a typical heterodyne spectrum that demonstrates significant rejection of unwanted anti-Stokes and pump signals. Here we show nearly 50 dB

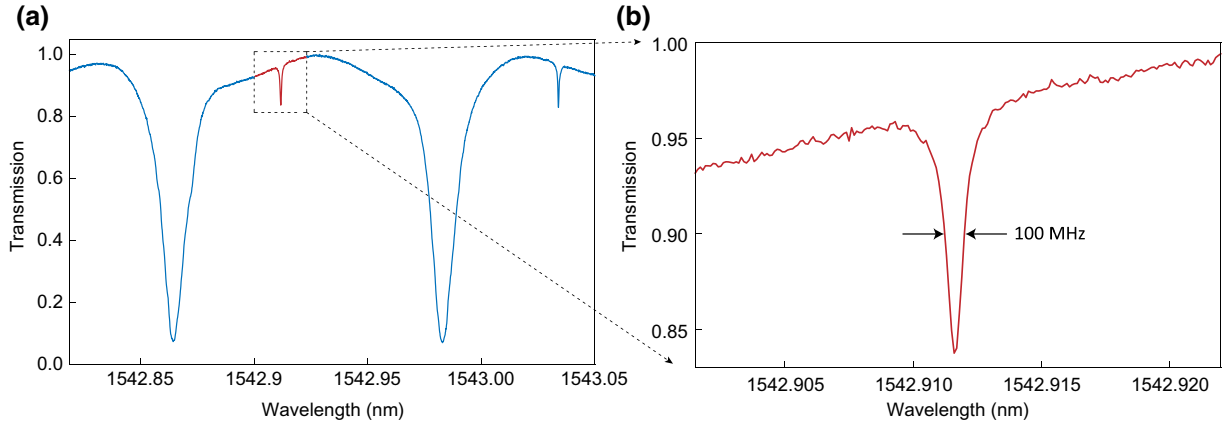

FIG. 6. (a) Characteristic multimode transmission spectrum measured at the thru port of coupler C (MC2). The broad (narrow) resonances are produced by the antisymmetric (symmetric) spatial mode. (b) Enlarged spectrum of a cavity resonance produced by the symmetric cavity mode, demonstrating an optical Q factor of nearly 2×10^6.

of anti-Stokes suppression, which results from the intrinsic phase-matching induced symmetry breaking between the Stokes and the anti-Stokes phonon wavevectors (i.e., $q_{\mathrm{as}} \neq q_s$) and the frequency selectivity of the cavity (i.e., $\omega_{\mathrm{as}} \neq \omega_2^m$).

As evident by the heterodyne spectrum displayed in Fig. 7, the transmitted pump light is also dramatically reduced thanks to the performance of the mode-specific couplers. Normalizing by the local oscillator power, only 1 part in 10^5 of the intracavity pump light exits the mode-specific coupler, reducing the transmitted pump powers significantly below the emitted Stokes powers.

APPENDIX D: FABRICATION

We demonstrate injection locked Brillouin lasing in racetrack resonators with circumferences of 15.7 and 5.1 mm that are respectively fabricated using a standard

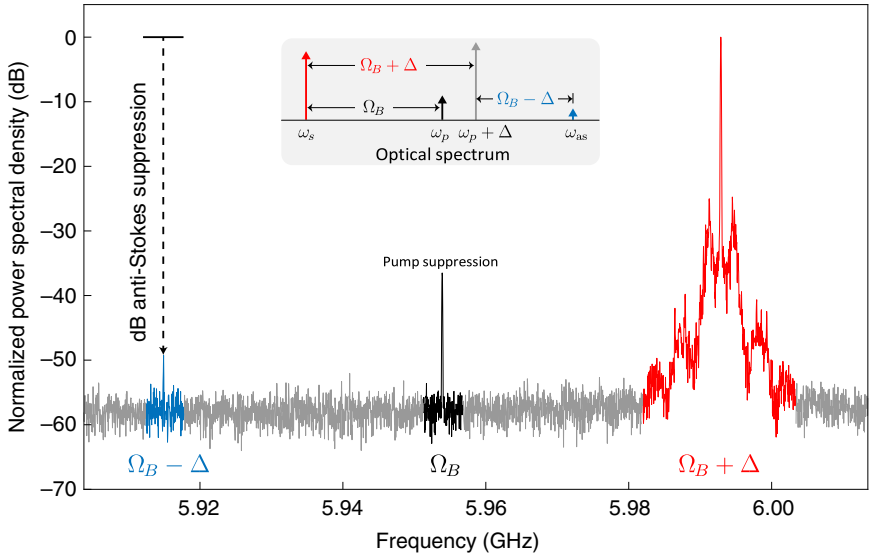

FIG. 7. Measured heterodyne power spectrum demonstrating large anti-Stokes and pump suppression [the experimental apparatus is diagrammed in Fig. 2(a) of the main text]. Here, the Brillouin laser is not injection locked. The inset diagrams the optical tones that produce three distinct microwave signals at $\Omega_B + \Delta$, Ω_B, and $\Omega_B - \Delta$, where Δ is the offset frequency of the optical LO. In this heterodyne configuration, emitted Stokes radiation interferes with the frequency-shifted LO to produce a beat note at $\Omega_B + \Delta$ (red). Note the characteristic fringes of the subcoherence spectrum that arise from a small delay between the signal and LO [27,51]. The Stokes light can also interfere with residual pump light to produce a beat note at Ω_B (black), while the anti-Stokes light beating with the optical LO yields a tone at $\Omega_B - \Delta$ (blue). From this spectrum, we observe record large 49 dB of anti-Stokes suppression. Considering the strength of the optical LO, this spectrum also demonstrates nearly 50 dB of pump suppression relative to the intracavity pump power.

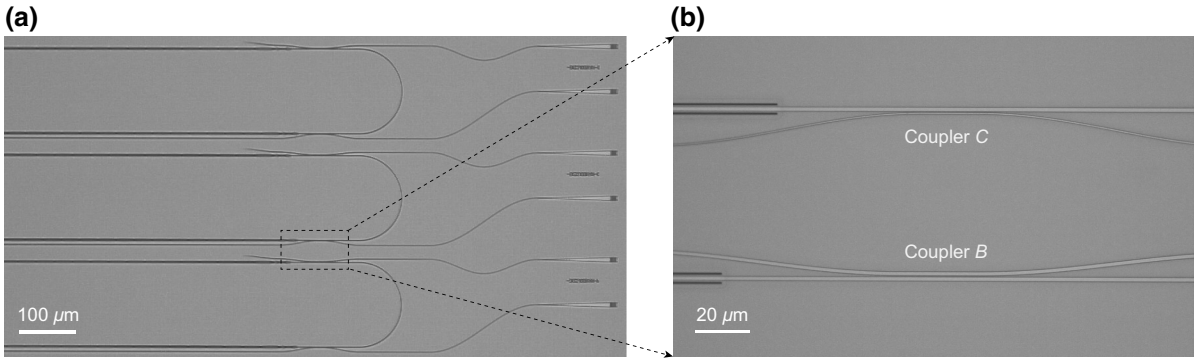

FIG. 8. Optical micrographs (gray scale) showing (a) the scale of the silicon Brillouin lasers and (b) an enlarged image of couplers *B* and *C*.

electron-beam lithography (for details, see the supplementary information of Ref. [29]) and CMOS-foundry photolithography processes. Data presented in Fig. 2 of the main text is obtained on the 15.7-mm-long device, which is interfaced with two couplers (couplers *B* and *C*). In this case, seed light enters the cavity through coupler *C*. The shorter devices, which are fabricated with CMOS photolithography, possess three couplers, as detailed in Fig. 1(a) of the main text. This device design is used to obtain the nonreciprocal data in Fig. 3 of the main text.

Figure 8 contains optical micrographs of the CMOS-fabricated devices, which are fabricated using Sandia National Laboratories' MESA facilities. We complete the fabrication process through a hydrofluoric-acid wet etch to remove the oxide undercladding. In Fig. 8(a) we show several Brillouin laser devices, while panel (b) highlights the mode-specific couplers *B* and *C*, which are designed to preferentially couple to the symmetric and antisymmetric spatial modes.

[1] B. K. Mathason and P. J. Delfyett, Pulsed injection locking dynamics of passively mode-locked external-cavity semiconductor laser systems for all-optical clock recovery, J. Lightwave Technol. **18**, 1111 (2000).

[2] Sang Eon Park, Taeg Yong Kwon, and Ho Seong Lee, Production of Raman laser beams using injection-locking technique, IEEE Trans. Instrum. Meas. **52**, 277 (2003).

[3] Katarzyna Balakier, Martyn J. Fice, Lalitha Ponnampalam, Alwyn J. Seeds, and Cyril C. Renaud, Monolithically integrated optical phase lock loop for microwave photonics, J. Lightwave Technol. **32**, 3893 (2014).

[4] Katarzyna Balakier, Lalitha Ponnampalam, Martyn J. Fice, Cyril C. Renaud, and Alwyn J. Seeds, Integrated semiconductor laser optical phase lock loops, IEEE J. Sel. Topics Quantum Electron. **24**, 1 (2017).

[5] Zujie Fang, Haiwen Cai, Gaoting Chen, and Ronghui Qu, *Single Frequency Semiconductor Lasers* (John Wiley & Sons, Bellingham, Washington USA, 2017), Vol. 1.

[6] Kaneyuki Kurokawa, Injection locking of microwave solid-state oscillators, Proc. IEEE **61**, 1386 (1973).

[7] Carl J. Buczek, Robert J. Freiberg, and M. L. Skolnick, Laser injection locking, Proc. IEEE **61**, 1411 (1973).

[8] Mian Zhang, Gustavo S. Wiederhecker, Sasikanth Manipatruni, Arthur Barnard, Paul McEuen, and Michal Lipson, Synchronization of Micromechanical Oscillators Using Light, Phys. Rev. Lett. **109**, 233906 (2012).

[9] Behzad Razavi, A study of injection locking and pulling in oscillators, IEEE J. Solid-State Circuits **39**, 1415 (2004).

[10] H. L. Stover and W. H. Steier, Locking of laser oscillators by light injection, Appl. Phys. Lett. **8**, 91 (1966).

[11] M. Sasnett, Injection-locked laser stabilizer, U.S. Patent No. 3,747,004 (1973).

[12] Roy Lang, Injection locking properties of a semiconductor laser, IEEE J. Quantum Electron. **18**, 976 (1982).

[13] Rongqing Hui, Alessandro D'Ottavi, Antonio Mecozzi, and Paolo Spano, Injection locking in distributed feedback semiconductor lasers, IEEE J. Quantum Electron. **27**, 1688 (1991).

[14] Mani Hossein-Zadeh and Kerry J. Vahala, Observation of injection locking in an optomechanical RF oscillator, Appl. Phys. Lett. **93**, 191115 (2008).

[15] Christiaan Bekker, Rachpon Kalra, Christopher Baker, and Warwick P. Bowen, Injection locking of an electro-optomechanical device, Optica **4**, 1196 (2017).

[16] Mitsuhiro Teshima, Kenji Sato, and Masafumi Koga, Experimental investigation of injection locking of fundamental and subharmonic frequency-modulated active mode-locked laser diodes, IEEE J. Quantum Electron. **34**, 1588 (1998).

[17] W. Liang, V. S. Ilchenko, D. Eliyahu, A. A. Savchenkov, A. B. Matsko, D. Seidel, and L. Maleki, Ultralow noise miniature external cavity semiconductor laser, Nat. Commun. **6**, 7371 (2015).

[18] Kun-Yii Tu, Mahmoud S. Rasras, Douglas M. Gill, Sanjay S. Patel, Young-Kai Chen, Alice E. White, Andrew Pomerene, Daniel Carothers, James Beattie, Mark Beals, *et al.* Silicon RF-photonic filter and down-converter, J. Lightwave Technol. **28**, 3019 (2010).

[19] Todd Lyndell Gustavson, Ph.D. thesis, Stanford University, 2000.

[20] Tara M. Fortier, Y. Le Coq, J. E. Stalnaker, Davi Ortega, Scott A. Diddams, Christopher W. Oates, and L. Hollberg, Kilohertz-Resolution Spectroscopy of Cold Atoms with

an Optical Frequency Comb, Phys. Rev. Lett. **97**, 163905 (2006).

[21] P Bouyer, T. L. Gustavson, K. G. Haritos, and M. A. Kasevich, Microwave signal generation with optical injection locking, Opt. Lett. **21**, 1502 (1996).

[22] Li Fan, Guangqiong Xia, Jianjun Chen, Xi Tang, Qing Liang, and Zhengmao Wu, High-purity 60 GHz band millimeter-wave generation based on optically injected semiconductor laser under subharmonic microwave modulation, Opt. Express **24**, 18252 (2016).

[23] Mengyue Shi, Lilin Yi, and Weisheng Hu, High-resolution Brillouin optoelectronic oscillator using high-order sideband injection-locking, IEEE Photon. Technol. Lett. **31**, 513 (2019).

[24] Luc Thévenaz, S. Le Floch, D. Alasia, and J. Troger, Novel schemes for optical signal generation using laser injection locking with application to Brillouin sensing, Meas. Sci. Technol. **15**, 1519 (2004).

[25] Vincent Jude Urick, Keith J. Williams, and Jason D. McKinney, *Fundamentals of Microwave Photonics* (John Wiley & Sons, Hoboken, New Jersey USA, 2015), Vol. 1.

[26] Katarzyna Balakier, Martyn J. Fice, Frederic van Dijk, Gael Kervella, Guillermo Carpintero, Alwyn J. Seeds, and Cyril C. Renaud, Optical injection locking of monolithically integrated photonic source for generation of high purity signals above 100 GHz, Opt. Express **22**, 29404 (2014).

[27] Nils T. Otterstrom, Ryan O. Behunin, Eric A. Kittlaus, Zheng Wang, and Peter T. Rakich, A silicon Brillouin laser, Science **360**, 1113 (2018).

[28] Eric A. Kittlaus, Nils T. Otterstrom, and Peter T. Rakich, On-chip inter-modal Brillouin scattering, Nat. Commun. **8**, 15819 (2017).

[29] Nils T. Otterstrom, Eric A. Kittlaus, Shai Gertler, Ryan O. Behunin, Anthony L. Lentine, and Peter T. Rakich, Resonantly enhanced nonreciprocal silicon Brillouin amplifier, Optica **6**, 1117 (2019).

[30] Heedeuk Shin, Wenjun Qiu, Robert Jarecki, Jonathan A. Cox, Roy H. Olsson III, Andrew Starbuck, Zheng Wang, and Peter T. Rakich, Tailorable stimulated Brillouin scattering in nanoscale silicon waveguides, Nat. Commun. **4**, 1944 (2013).

[31] Raphaël Van Laer, Bart Kuyken, Dries Van Thourhout, and Roel Baets, Interaction between light and highly confined hypersound in a silicon photonic nanowire, Nat. Photonics **9**, 199 (2015).

[32] Eric A. Kittlaus, Heedeuk Shin, and Peter T. Rakich, Large Brillouin amplification in silicon, Nat. Photonics **10**, 463 (2016).

[33] P. St. J. Russell, D. Culverhouse, and F. Farahi, Experimental observation of forward stimulated Brillouin scattering in dual-mode single-core fibre, Electron. Lett. **26**, 1195 (1990).

[34] Myeong Soo Kang, A. Brenn, and P. St. J. Russell, All-Optical Control of Gigahertz Acoustic Resonances by Forward Stimulated Interpolarization Scattering in a Photonic Crystal Fiber, Phys. Rev. Lett. **105**, 153901 (2010).

[35] Robert W. Boyd, *Nonlinear Optics* (Elsevier, San Diego, California USA, 2003).

[36] Shai Gertler, Prashanta Kharel, Eric A. Kittlaus, Nils T. Otterstrom, and Peter T. Rakich, Shaping nonlinear optical response using nonlocal forward Brillouin interactions, arXiv:1909.08129 (2019).

[37] Myeong Soo Kang, A. Butsch, and P. St. J. Russell, Reconfigurable light-driven opto-acoustic isolators in photonic crystal fibre, Nat. Photonics **5**, 549 (2011).

[38] Elias Giacoumidis, Amol Choudhary, Eric Magi, David Marpaung, Khu Vu, Pan Ma, Duk-Yong Choi, Steve Madden, Bill Corcoran, Mark Pelusi *et al.*, Chip-based Brillouin processing for carrier recovery in self-coherent optical communications, Optica **5**, 1191 (2018).

[39] Radan Slavík, Zhixin Liu, and David J. Richardson, in *Optical Fiber Communication Conference* (Optical Society of America, Los Angeles, California USA, 2017), p. Th4I–3.

[40] Nicholas C. Harris, Yangjin Ma, Jacob Mower, Tom Baehr-Jones, Dirk Englund, Michael Hochberg, and Christophe Galland, Efficient, compact and low loss thermo-optic phase shifter in silicon, Opt. Express **22**, 10487 (2014).

[41] A. Kodigala, M. Gehl, C. T. DeRose, D. Hood, A. T. Pomerene, C. Dallo, D. Trotter, P. Moore, A. L. Starbuck, J. Lee *et al.*, in *CLEO: Science and Innovations* (Optical Society of America, San Jose, California USA, 2019), p. STh4N–6.

[42] Christopher G. Poulton, Ravi Pant, Adam Byrnes, Shanhui Fan, M. J. Steel, and Benjamin J. Eggleton, Design for broadband on-chip isolator using stimulated Brillouin scattering in dispersion-engineered chalcogenide waveguides, Opt. Express **20**, 21235 (2012).

[43] JunHwan Kim, Mark C. Kuzyk, Kewen Han, Hailin Wang, and Gaurav Bahl, Non-reciprocal Brillouin scattering induced transparency, Nat. Phys. **11**, 275 (2015).

[44] Freek Ruesink, Mohammad-Ali Miri, Andrea Alu, and Ewold Verhagen, Nonreciprocity and magnetic-free isolation based on optomechanical interactions, Nat. Commun. **7**, 13662 (2016).

[45] Dimitrios L. Sounas and Andrea Alù, Non-reciprocal photonics based on time modulation, Nat. Photonics **11**, 774 (2017).

[46] Ewold Verhagen and Andrea Alù, Optomechanical nonreciprocity, Nat. Phys. **13**, 922 (2017).

[47] Donggyu B. Sohn, Seunghwi Kim, and Gaurav Bahl, Time-reversal symmetry breaking with acoustic pumping of nanophotonic circuits, Nat. Photonics **12**, 91 (2018).

[48] Eric A. Kittlaus, Nils T. Otterstrom, Prashanta Kharel, Shai Gertler, and Peter T. Rakich, Non-reciprocal interband Brillouin modulation, Nat. Photonics **12**, 613 (2018).

[49] Yuya Shoji, Tetsuya Mizumoto, Hideki Yokoi, I-Wei Hsieh, and Richard M. Osgood, Jr., Magneto-optical isolator with silicon waveguides fabricated by direct bonding, Appl. Phys. Lett. **92**, 071117 (2008).

[50] Duanni Huang, Paolo Pintus, Chong Zhang, Yuya Shoji, Tetsuya Mizumoto, and John E. Bowers, Electrically driven and thermally tunable integrated optical isolators for silicon photonics, IEEE J. Sel. Top. Quantum Electron. **22**, 4403408 (2016).

[51] L. Richter, H. Mandelberg, M. Kruger, and P. McGrath, Linewidth determination from self-heterodyne measurements with subcoherence delay times, IEEE J. Quantum Electron. **22**, 2070 (1986).